Annu. Rev. Phys. Chem. 1999. 50:279–313

APPLICATIONS OF IMPULSIVE STIMULATED SCATTERING IN THE EARTH AND PLANETARY SCIENCES

E. H. Abramson,[1] J. M. Brown,[2] and L. J. Slutsky[1]
[1]*Department of Chemistry and the* [2]*Geophysics Program, University of Washington, Seattle, Washington 98195; e-mail: evan@geophys.washington.edu; brown@geophys.washington.edu; slutsky@macmail.chem.washington.edu*

Key Words Brillouin spectroscopy, high pressure, mantle minerals, diamond-anvil cell, thermal diffusivity, equation of state, seismic velocities

■ **Abstract** The elastic, thermodynamic, and transport properties of crystals and fluids at high temperature and pressure play a central role in the earth and planetary sciences as well as in a variety of technologies. These properties also constitute a principal experimental constraint on the description of intermolecular interactions at short distances. Aspects of "impulsive stimulated scattering," when adapted to measurements in the diamond-anvil high-pressure cell, provide an approach to the determination of a subset of equilibrium and dynamic properties at high density.

INTRODUCTION

The elastic, thermodynamic, and transport properties of crystals and fluids at high temperature and pressure play a central role in the earth and planetary sciences as well as in a variety of technologies. These properties also constitute a principal experimental constraint on the description of intermolecular interactions at short distances. Aspects of "impulsive stimulated scattering," when adapted to measurements in the diamond-anvil high-pressure cell provide an approach to the determination of a subset of equilibrium and dynamic properties at high density.

The propagation parameters of longitudinal and transverse elastic waves and Earth's free oscillations are the principal probes into the structure of the otherwise inaccessible deep interior. The average radial seismic profile, based on wave travel times and mode frequencies (1), has been augmented with recently imaged lateral structure using tomographic reconstruction methods (2). The interpretation of such three-dimensional seismic structure in terms of temperature, mineral phase, and chemical composition requires knowledge of the acoustic velocities in the

0066-426X/99/1001-0279$08.00

candidate phases at appropriately strenuous conditions of temperature and pressure (3, 4).

Questions of thermal heterogeneity in Earth versus heterogeneity in terms of mineral phases and the elemental composition cannot be satisfactorily addressed on the basis of estimated properties of candidate mantle constituents. The most direct application of impulsively stimulated scattering to the earth sciences has been as part of the effort to construct a more soundly based experimental foundation for the conversion of seismic images to thermal and mineralogical profiles. These techniques, as well as ultrasonics in multi-anvil high-pressure systems (5) and conventional Brillouin spectroscopy (6), allow determination of elastic constants and equations of state. Representatives of each of the principal classes of upper-mantle minerals have now been examined at pressures equal to or higher than those at the 410-km discontinuity. Some temperature derivatives of the elastic moduli at high pressure have also been measured in large volume apparatuses and by impulsive stimulated scattering in the diamond-anvil cell. These results and their implications for the earth sciences are considered.

Beyond the definition of the chemical and thermal structure of the mantle, the lack of firm experimental or theoretical constraints on material properties at high pressure is a major barrier to successful modeling of fundamental processes in Earth and in the major planets. Heterogeneity of density (associated with both temperature and compositional differences) constitutes the driving force for mantle convection and plate tectonics. A valid description of such planetary-scale dynamics rests on knowledge of the equation of state, thermal transport properties, and viscoelastic behavior of mantle candidate minerals at high pressure. At modest depths, water circulation transports heat and mass from hot magma bodies to the surrounding rock and to the surface. The physical and chemical properties of ionic solutions at elevated temperatures and pressures (equations of state, chemical potentials, activity coefficients) play a central role in a description of, for example, ore deposition and processes at mid-ocean spreading centers. Application of impulsive stimulated scattering to the measurement of thermal diffusivity, chemical potentials of solute species, and viscoelastic properties is therefore considered here.

Even though the range of pressures and temperatures accessible by experiment has expanded, genuinely extreme conditions in Earth and especially in the giant planets (7) remain beyond the reach of current technology. Under such conditions or in chemically rigorous environments (associated, for example, with the behavior of water in the upper mantle), computational theory based on empirical potentials or quantum mechanical methods, validated by experiment at intermediate temperatures and pressures, would seem to be the most immediately promising predictive resource.

Outside a geophysical context, the description of processes at ambient pressures, high-speed impact, sputtering, the rate of passage over steric barriers to reaction, and diffusion also rests on knowledge of internuclear potentials at distances longer than covalent bonds but considerably shorter than nonbonded contacts at ambient conditions. Although there is an extensive body of information and theory on such

interactions near the potential minimum, the regime of strong repulsive interactions at very high densities has not been extensively investigated (8).

The high-pressure equation of state has been the principal experimental probe into intermolecular interactions in the repulsive region. X-ray crystallography in the diamond-anvil cell permits study of solids; fluids are experimentally more difficult. Two-body central-force potentials, on occasion augmented by the Axilrod-Teller (9) three-body interaction, have successfully reproduced the equation of state of a number of highly symmetric solids. However, theoretical estimates of three-body exchange interactions (9, 10) predict a significant deviation from purely pair repulsive potentials even at distances corresponding to moderate pressures. The failure of the Cauchy relations between the elastic constants of crystals where each atom or ion occupies a center of symmetry reinforces this point. It has been argued persuasively (11, 12) that the role of the many-body exchange interaction in those deformations that preserve the high site symmetry of simple crystal structures, and thereby minimize the distortion of atomic or molecular wave functions, is relatively small. Thus, an approach to the interaction energy that reproduces the pressure-density relation of a crystal cannot be transferred with confidence to less-symmetrical situations. Data on fluids and on the tensorial properties of simple crystals should then provide a more rigorous environment for the confrontation of theoretical approaches with experiment. Constraints on model potentials both for water and for a few simple fluids and crystals are therefore briefly discussed.

EXPERIMENTAL METHODS

The Acoustic Grating

Thermally stimulated Brillouin spectroscopy as a particular aspect of impulsive stimulated scattering is reviewed by Fayer (13, 14) and by Yan et al (15) and, more specifically in the context of experiments in the diamond-anvil cell, by Brown et al (16, 17). In outline, two excitation pulses are selected from the output train of a Q-switched, mode-locked laser and recombined in the sample at an angle 2θ, but otherwise coincident in space and time. Interference establishes a periodic distribution of intensity. In a sample that absorbs at the wavelength of the excitation pulses, a (spatially) periodic variation in the temperature ensues. In a general crystallographic direction in an anisotropic crystal, the associated thermal pressure will launch one quasilongitudinal and two quasitransverse acoustic waves; in an isotropic medium, only a single longitudinal mode is observed. In samples that do not exhibit resonant optical absorption at the laser frequency, electrostriction constitutes an alternate mechanism for the excitation of acoustic phonons. In either case, the acoustic wavelength, λ_A, expressed in terms of λ, the wavelength of the laser light and θ, is equal to the grating spacing, d,

$$d = \lambda_A = \frac{\lambda}{2\sin(\theta)}. \qquad 1.$$

The impulsively excited acoustic waves induce a temporally and spatially periodic variation in the index of refraction of the sample. A third pulse, selected from the same Q-switched envelope as the excitation pulses, can be frequency doubled and delayed by time of flight to generate a probe. Observation of the intensity of the Bragg scattering of the probe by the acoustic grating as a function of probe delay serves to determine the frequency (f_A), and hence the velocity ($c = \lambda_A f_A$), as well as the attenuation of the acoustic waves. A time-domain record for the scattering of a 532-nm probe from a grating excited by 80-ps, 1064-nm pulses in a single crystal of olivine is given in Figure 1*a*. The sample was loaded to a pressure of 4.6 GPa in a diamond-anvil cell with argon as a pressure-transmitting medium and a ruby fluorescence pressure standard. Both the quasilongitudinal and one of the two quasitransverse modes are apparent as sharp peaks in the power spectrum of this record (Figure 1*b*).

Figure 2 is a schematic illustration of the geometry of the experiment in the diamond-anvil cell. The wave vector of the optically excited acoustic phonons is vertical and in the plane of the drawing. In much of the work considered here, the cell is mounted in a vacuum oven. In studies of crystalline samples, the cell, or the

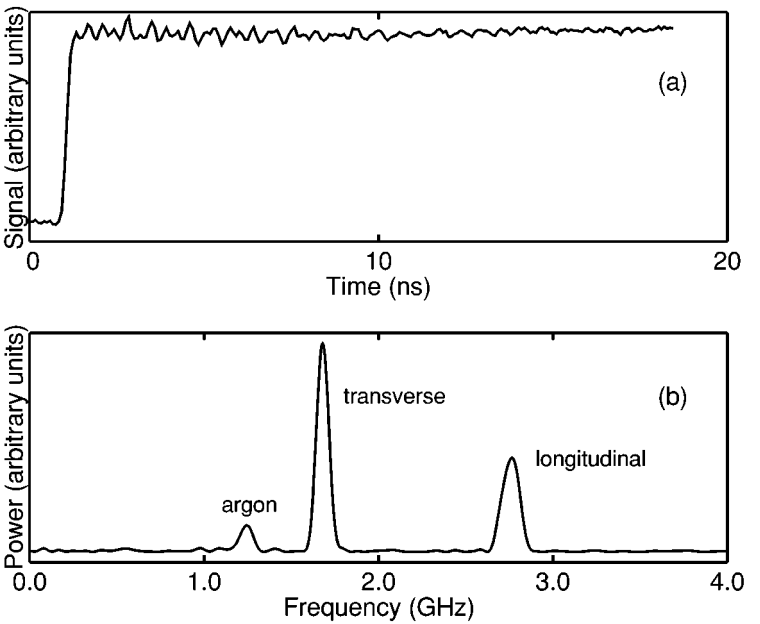

Figure 1 (*a*) The Bragg-diffracted scattering from a sample of olivine in the diamond-anvil cell at 4.6 GPa and 250°C. The signal is modulated by impulsively stimulated acoustic waves. (*b*) The power spectrum of the signal shows the quasilongitudinal wave and one of the two quasitransverse waves in the olivine; also seen is the quasilongitudinal wave in the pressure-transmitting medium, argon. With a wavelength of 3.086 μm, the signals correspond to velocities of 8.510, 5.184, and 3.845 km s^{-1}.

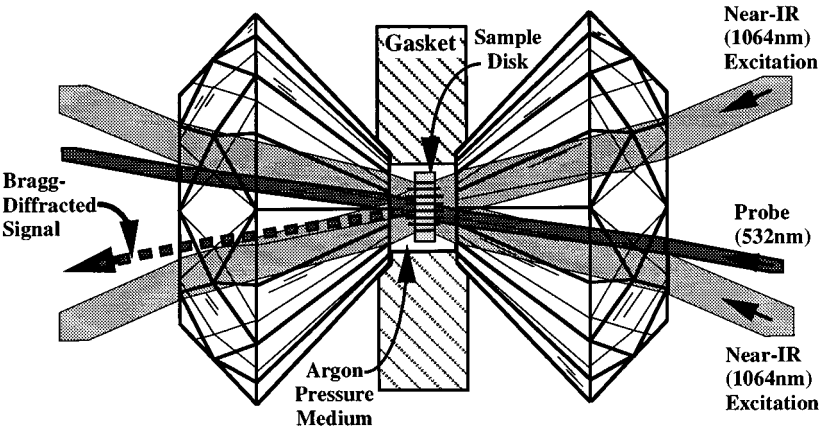

Figure 2 The diamond-anvil cell comprises two diamonds that are pressed by backing plates (not shown) into a metal gasket (e.g. steel, rhenium) to form a high-pressure seal. A mineral sample is typically loaded as a disk 200 μm in diameter and 20–70 μm thick, with optically polished faces. Optical access is through the backs of the diamonds and corresponding holes in the backing plates.

oven and cell, are rotated around the horizontal axis of the figure. Measurement of the acoustic velocity as a function of the direction of propagation then permits the determination of the elastic constants of a crystal. A typical result of this procedure, for an olivine single crystal, is given in Figure 3.

Accurate work requires that there be many cycles of the grating in the volume illuminated by the probe. The sample sizes used are typically about 200 μm in breadth, with a thickness of several tens of microns. If, at a workable acoustic wavelength, the acoustic frequency is not so high as to tax the time resolution of conveniently available detectors and transient digitizing systems, a continuous probe can be utilized. In this case, the entire time-domain signal is observed for each shot of the excitation laser (18, 19). Employing this approach, Rogers & Nelson (18) measured the velocity and attenuation of ultrasonic waves in thin polymer films. They obtained excellent signal-to-noise with a single shot of the excitation laser system. Typical frequencies for elastic waves in the diamond-anvil cell, ranging past 3 GHz, challenge currently available detectors and recorders.

The Thermal Grating

When the acoustic disturbance has been fully damped, a spatially periodic distribution of temperature and hence index of refraction remains. This thermal grating decays exponentially. The rate constant, R, and time, τ, for the relaxation of the periodic distribution of temperature are given by

$$R = 1/\tau = \frac{4\pi^2 D}{d^2}, \qquad 2.$$

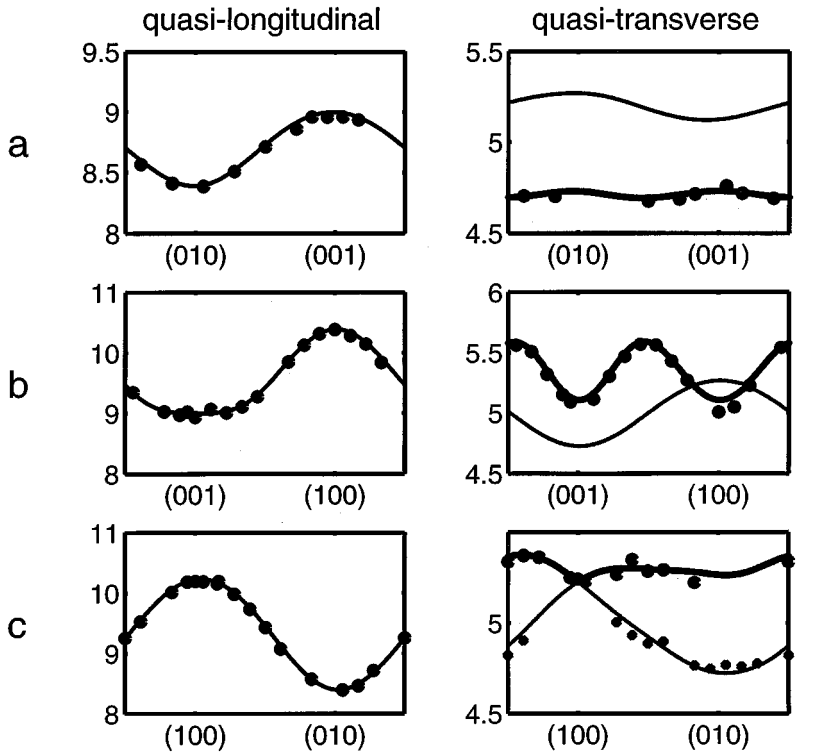

Figure 3 Sound velocities (vertical axis in kilometers per second) in olivine ($Mg_{1.8}Fe_{0.2}SiO_4$) at 10.4 GPa and 25°C are shown as functions of crystallographic direction. The data were taken from three different cuts of crystal, with principal faces nearly normal to the *a*, *b*, and *c* axes. Both the quasilongitudinal and the two quasitransverse branches are seen. (*Solid lines*) Velocities calculated as a result of adjusting the elastic constants of the crystal so as to give an optimal fit to the data. Those samples (*a* and *b*) that were cut within $\sim 2^\circ$ of the principal axes do not allow efficient excitation of the vertically polarized transverse mode; data points are thus not exhibited on the corresponding curves.

where D is the thermal diffusivity (that is, the thermal conductivity divided by the heat capacity per unit volume) and d is the grating spacing. The variation of R with the angle of intersection of the excitation pulses, specified by Equations 1 and 2, serves to distinguish one-dimensional thermal diffusion from radiative loss or other relaxation processes. In Figure 4*a*, the scattering of a continuous argon-ion laser probe from a crystal of orthopyroxene is given as a function of time at several values of θ over a more extended range than that depicted in Figure 1. A plot of R versus d^{-2} derived from these data is shown in Figure 4*b*. Observation of the dependence of D on crystallographic direction then serves to specify all elements of the thermal diffusivity tensor of the crystal.

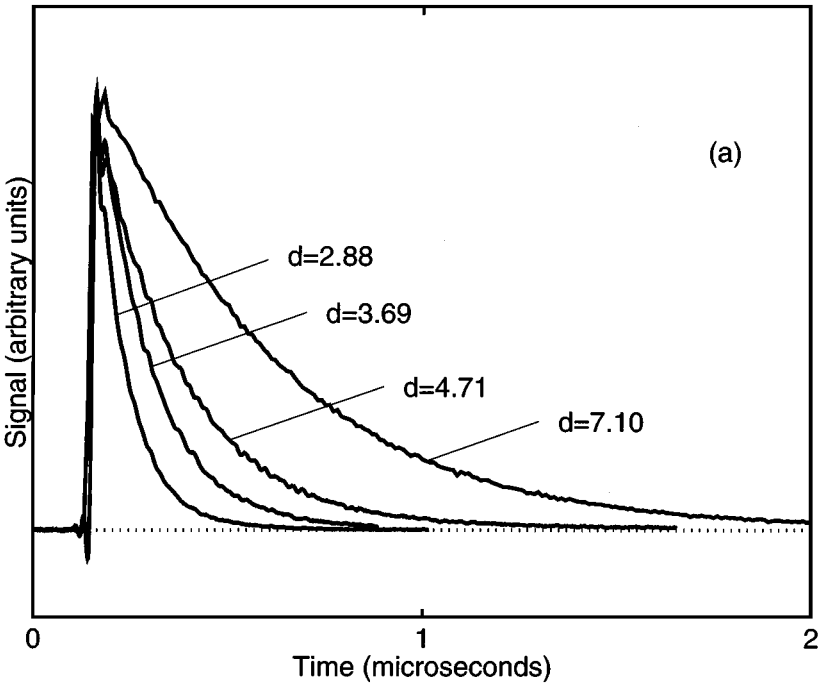

Figure 4 (*a*) After the acoustic disturbances have vanished, the thermal grating decays exponentially with a lifetime proportional to the square of the grating spacing (given in units of microns). The traces seen here are from an aluminous orthopyroxene, under ambient conditions, with heat flow along the crystallographic *a* axis.

Heterodyning

In the case of the data in Figure 1, the acoustic absorption is small and the thermal relaxation time is long enough so that the effect of the thermal grating can be represented by a time-independent contribution to the scattered amplitude. Thus, the simple form

$$I = \left(A_{th} - \sum_i A_{iac} \cos(\omega_i t) \right)^2, \qquad 3.$$

where A_{th} is the amplitude scattered by the thermal grating, A_{iac} is the amplitude scattered by the acoustic grating, and ω_i is the circular frequency of the *i*th acoustic mode ($\omega_i = 2\pi f_i$), will give a good account of the data. In Figure 1, mixing of the relatively weak electrostrictively excited acoustic signal in argon (a common hydrostatic pressure medium) with that from the strong thermal grating in the olivine sample produces a visible peak in the Fourier transform corresponding to the phonon frequency in argon. The higher amplitudes associated with thermoacoustic excitation can in this way be exploited in systems such as the inert gases, where the optical absorption is itself small.

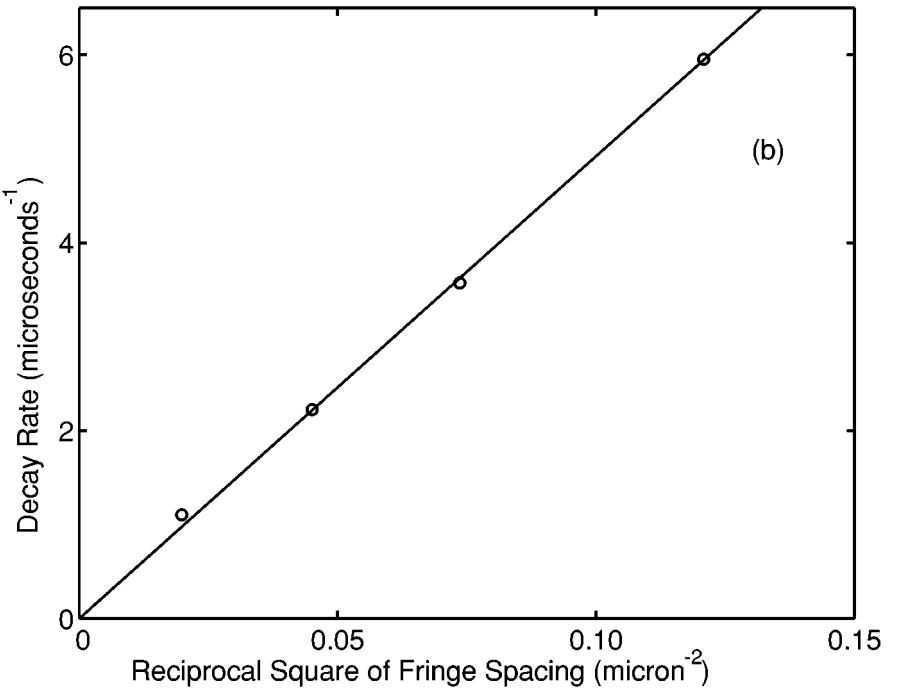

Figure 4 (*b*) The inverse lifetimes of the traces in Figure 4*a* are plotted against the inverse square of the grating spacing. The slope of the resulting line indicates a thermal diffusivity of $D = 1.25 \times 10^{-3}\,\mathrm{cm}^2\,\mathrm{s}^{-1}$.

Recently, Maznev et al (20) reported a simplified method for ensuring a stable phase relation between the diffracted probe and an external, heterodyning, reference beam. The signal is then proportional to $(I_P I_R)^{1/2}$, where I_R and I_P are, respectively, the intensities of the reference beam and the weakly-scattered probe. Their approach offers the prospect of a considerable increase in the sensitivity of the technique as well as improvement in the ease of optical alignment.

Surface Waves

The elastic constants of an anisotropic single crystal are implicit in the velocity of surface or interfacial acoustic waves as a function of crystallographic direction (21, 22). Coherent optical excitation and probing of interfacial waves (Stonely waves and leaky Rayleigh waves) at the boundary between an oriented metal crystal (or other optically opaque material) and the pressure-transmitting medium in a diamond-anvil cell can be used to determine the elastic constants of the metal as functions of temperature and pressure. A representative result for Rayleigh waves propagating in the (010) plane of a Ge single crystal is given in Figure 5.

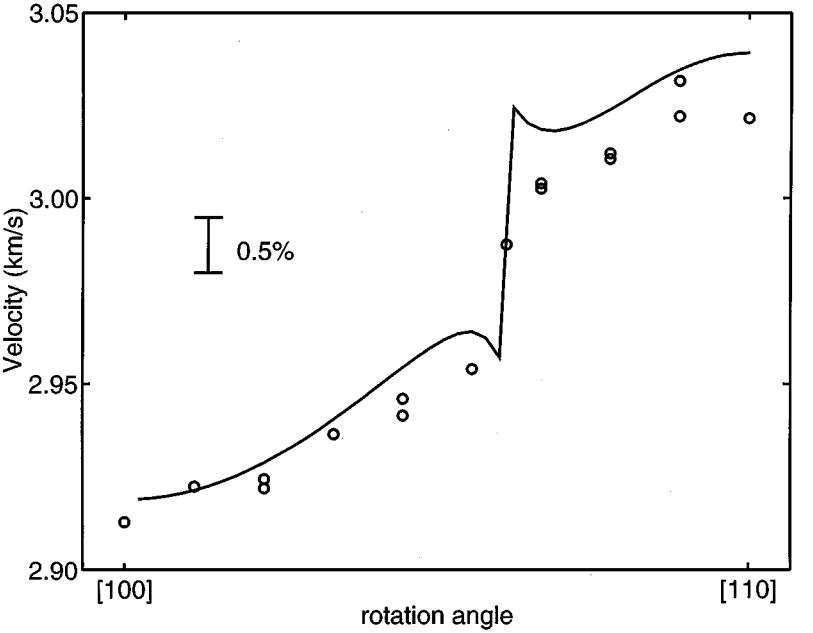

Figure 5 Rayleigh waves, as stimulated on the (010) surface of a crystal of germanium, lead to (reflective) surface diffraction of a probe beam. (*Circles*) Experimentally derived data for the velocities; (*smooth line*) calculated velocities based on literature values of the elastic constants.

Pressure Measurement

Modeling in service of the earth and planetary sciences requires data at simultaneously high pressure and high temperature or, lacking this, temperature derivatives at high pressure that can serve as the basis for extrapolation. Pressures in the diamond-anvil cell are commonly measured by ruby fluorescence (23–25); the calibration to pressures in excess of 100 GPa is given as (24)

$$P(\text{GPa}) = 380.8\left(\left(\frac{\lambda(P)}{\lambda(0)}\right)^5 - 1\right), \qquad 4.$$

where $\lambda(0)$ represents the wavelength of the peak of the R_1 fluorescence at ambient pressure and the temperature of the experiment, and $\lambda(P)$ is the peak wavelength for a ruby in the high-pressure cell at the same temperature.

The ruby fluorescence pressure scale is based on temperature derivatives of $\lambda(P)$ determined at ambient pressure and pressure derivatives determined near 298 K; the mixed partial derivative of $\lambda(P)$ with respect to T and P is not taken into account. Determination of the pressure dependence of the temperature derivatives of acoustic velocities, central to the interpretation of seismic profiles,

requires an estimate of the magnitude of the mixed partial derivative for the ruby scale.

Comparisons by Wunder & Schoen (26) of the melting line of water determined by Bridgman (27) with a determination based on the ruby scale indicates that the absolute and ruby scales agree to within ± 0.04 GPa at 160°C and 1.6 GPa. Independently, Vedam & Holton (28) have reported the velocity of sound in water to pressures of 0.98 GPa and temperatures of 80°C, and Grindley & Lind (29) determined the equation of state to 1.00 GPa and 150°C, both based on an absolute pressure scale. The results (28, 29), appropriately differentiated, determine the acoustic velocity as a function of temperature and pressure. Complementary measurements of stimulated Brillouin scattering in pure water (30), with pressure measured by ruby fluorescence, then allow a direct comparison of the ruby-fluorescence and absolute-pressure scales at modestly elevated temperatures. Such comparison indicates that the conventional implementation of the ruby scale (Equation 4) is accurate to better than 0.01 GPa below 150°C and 1.0 GPa.

Although ruby fluorescence is the most commonly used (optical) standard for the measurement of high pressure, it is far from ideal. In particular, the large temperature coefficient, for best accuracy, requires knowledge of the temperature of the ruby to within 1°C; this also precludes the use of high excitation powers and leads to weak signals. In addition, Al_2O_3 is reactive in such environments as aqueous solutions above $\sim$250°C.

Several other materials have been proposed as optical standards. Samarium has been doped into several different hosts, yielding fluorescence that shows a usefully small temperature dependence. In particular, the hosts yttrium-aluminum-garnet (31–33) and SrB_4O_7 (34, 35) show promise. The latter has the advantage of a sharp, single peak that remains uncluttered even at high temperatures. Neither is likely to be superior to ruby in a reactive environment. The Raman shift of ^{13}C diamond has also been used as a measure of pressure (36), and although the intensity is low and the signal merges with that of the diamond anvils at higher pressures, the temperature coefficient is small. Furthermore, diamond has the distinct advantage of being chemically inert. Progress toward higher temperatures rests primarily on the development of a more accurate and chemically stable optical pressure gauge.

MANTLE MINERALS

Overview

The Earth's mantle extends from the base of the crust, at an average depth of 35 km beneath the continents and 6 km beneath the oceans, to the core-mantle boundary at a depth of about 2900 km. The mantle contains about 68% of Earth's mass. Estimates of the bulk mantle chemistry rely on the assumption that Earth's composition is similar to that of the Sun (excluding H and He) and to the chondritic meteorites (37). Oxygen, silicon, and magnesium dominate the estimated bulk chemistry, and five elements (Si, Mg, Fe, Al, Ca) account for over 99%

of the cations. Mantle samples, brought up by deep-seated volcanic processes as rock fragments (xenoliths), give evidence for chemical heterogeneity in the upper 200 km of the mantle (38). This variability arises in part from chemical fractionation associated with partial melt. Fractional melting (approximately 10% of the mass) tends to concentrate incompatibles (Al, Ca, P, K) and silicon in the liquid. Melts ultimately add to the volume of Earth's crust, leaving a depleted mantle residuum, with reduced Si/Mg and Fe/Mg ratios. A fundamental problem in the earth sciences is to determine the degree of chemical fractionation and heterogeneity in regions not directly sampled by xenoliths.

On the basis of the seismic profiles (1), the mantle divides into three radial zones (upper mantle, transition zone, lower mantle) separated by discontinuities in velocity at average depths of 410 km and 660 km (39). The principal upper-mantle minerals are olivines $(Mg_{1-x}Fe_x)_2SiO_4$, orthopyroxenes $(Mg_{1-x}Fe_x)SiO_3$, clinopyroxenes $Ca(Mg_{1-x}Fe_x)Si_2O_6$, and $NaAl_2Si_2O_6$ and garnets $(Ca, Mg_{1-x}Fe_x)_3Al_2Si_3O_{12}$. These formulas are, however, approximate; extensive substitution occurs in response to variations in pressure, temperature, and chemical environment. Over a range of pressure extending from the upper mantle into the transition zone, the pyroxene component reequilibrates within a majorite garnet solid solution (40). Olivine transforms to wadsleyite (β-phase) under conditions appropriate to the 410-km seismic discontinuity. At pressures near 23 GPa (660 km), the silicates of the upper mantle with fourfold coordinated silicon convert to (Mg,Fe)O and the perovskite structure with sixfold coordination of silicon. The details of elemental partitioning and phase equilibria under lower-mantle pressure-temperature conditions are under investigation (41–43).

The variation of pressure and temperature with depth in the mantle is illustrated in Figure 6. The pressure is determined by integration of the known mass distribution (1). The temperature profile is less certain. Convective motion within the solid, but ductile, mantle transports heat to Earth's surface. In the convective interior, the adiabatic temperature gradient $(\partial T/\partial P)_s$ is implicit in the assumed equation of state, which in turn is based on the equations of state of the constituent minerals and the analysis of the seismic profile in terms of mineral composition.

Estimates place the adiabatic gradient between 0.3 and 0.5°C/km (44). Studies of the coexistence curve of tetrahedral silicates with six-coordinate silicates and shock wave determinations of the melting curve of iron provide additional constraints at, respectively, 660 km and the boundary between the solid and liquid core. Conductive boundary layers, which must exist at the top and bottom of the mantle, have gradients of several tens of degrees per kilometer. Extended measurement of the thermal diffusivity of the mantle candidate minerals will serve to characterize these gradients more precisely.

The range of temperatures corresponding to the upper mantle is not fully accessible in the externally heated diamond-anvil cell. However, it has been possible to measure the effect of pressure on the temperature derivative of the velocity and thus to provide a sounder basis for extrapolation than has heretofore been possible. The experiments reviewed here seek to determine accurate sound velocities, equations-of-state, and thermal diffusivities for all major constituents of the

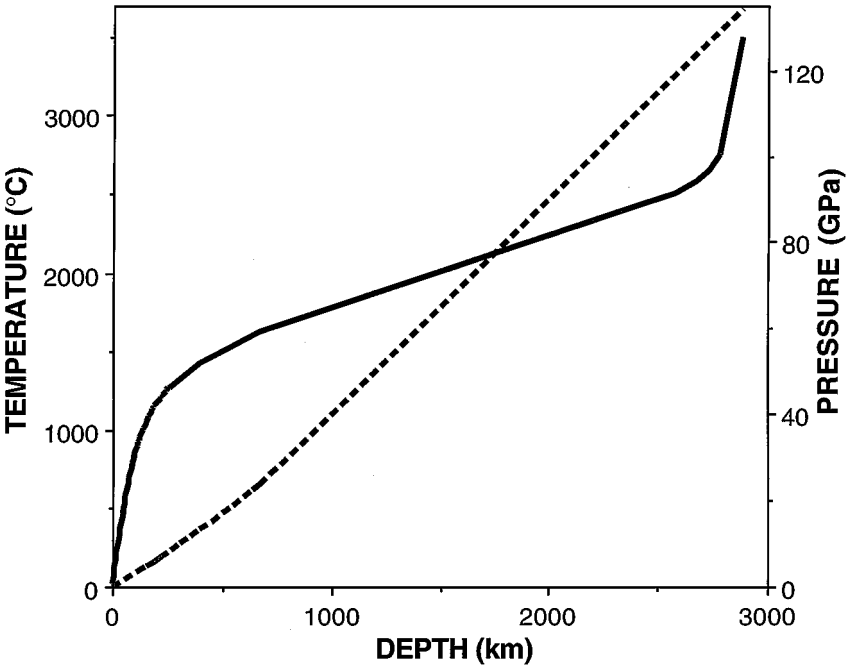

Figure 6 Mantle temperatures (*solid line, left-hand scale*) and pressures (*dashed line, right-hand scale*) as functions of depth.

mantle. The broader goal is to provide data that form a more secure basis for interpretation of Earth processes. Single crystal properties are appropriately averaged and mixed to estimate the elastic properties of a polycrystalline aggregate (45). The overall picture that emerges from these experiments is significantly different from the standard model based on extrapolation of mineral properties relying on pressure and temperature derivatives determined near ambient pressure.

Acoustic Velocities and Equations of State

Both olivine and orthopyroxene crystallize in the orthorhombic system with nine independent elastic constants and three independent diagonal components of the thermal diffusivity tensor. Garnet is cubic with three independent elastic constants and scalar thermal diffusivity. The monoclinic clinopyroxenes have 13 elastic constants and 4 thermal diffusivity components.

The elastic secular equation is

$$|A_{ij} - \rho c^2 \mathbf{I}| = \mathrm{O}, \qquad 5.$$

where $\mathbf{I}$ is the 3×3 unit matrix, ρ is the density, c is the speed of sound, and the elements of $\mathbf{A}$ are functions of the elastic constants and of the direction of propagation of the sound waves in question (46, 46a, 48).

The elastic constants are determined by an adjustment of the parameters of Equation 5 so as to optimally describe the measured velocities as functions of crystallographic orientation. In Brown et al (16, 46, 47, 48), samples with principal faces perpendicular to the *a*, *b*, and *c* crystal axes were employed, providing redundant constraints on the constants and reducing the maximum number of variables required to describe an individual data set, such as those in Figure 3.

As the pressure is increased, preliminary values of the elastic constants and hence an approximate adiabatic compressibility can be derived from Equation 5 and known densities at lower pressure. The small (∼1%) correction from adiabatic to isothermal moduli can be made using ambient pressure properties. The value of the density is then recursively refined until convergence is achieved. The result of this procedure for an iron-bearing olivine at 298 K is compared with the crystallographic studies of Kudoh & Takeuchi (49) in Figure 7 as well as with a density-functional based calculation by Brodholt et al (50). In the common range of pressure, the acoustically determined equation of state agrees with the X-ray measurements within the error of the latter. Zha et al (51) recently extended the

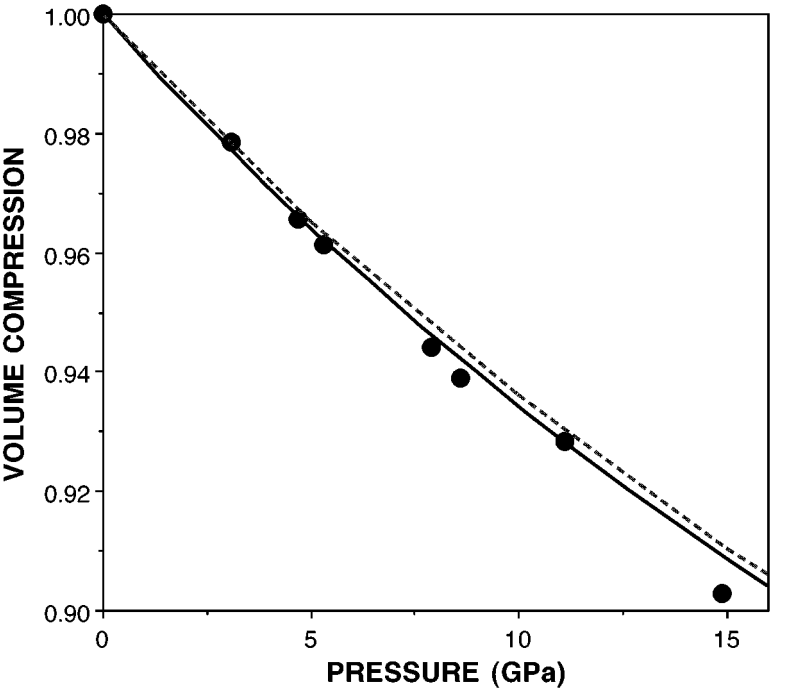

Figure 7 The fractional volume compression of olivine at 25°C derived from the elastic constants measured by thermally stimulated Brillouin scattering (*continuous curve*) and from X-ray crystallography (*points*). (*Broken curve*) The results of a density-functional calculation by Brodholt & Wood (89).

comparison to 32 GPa (and concluded also that the ruby-based pressure scale is in reasonable accord with the data). Similar agreement has been noted for a pyrope-rich garnet (52) to 25 GPa.

Any relaxation process with characteristic frequency between 0 and 3 GHz that has a significant effect on the compressional and off-diagonal compliances would lead to a discrepancy between the essentially static crystallographic measurement and the lattice parameters derived from impulsive stimulated scattering. The close correspondence between the two data sets in Figure 7 supports but does not establish the transferability of the high-frequency moduli to the analysis of low-frequency seismic data. It would of course still be possible to adduce a process that, at room temperature, is slow even on the very slow time scale of the crystallographic investigations but with a relaxation frequency that lies between seismic and ultrasonic frequencies at mantle conditions. Agreement between a high-temperature crystallographic isotherm and an acoustic equation of state at elevated temperature would add to the confidence with which one might transfer laboratory data to a geophysical context.

Mantle Elasticity

Previous interpretation of the seismic structure of Earth has, to a large extent, been based on elasticity data taken at low pressure for a restricted range of mineral composition. Assumption of a linear relation between moduli and pressure has been a prevailing approach. Temperature derivatives at high pressure have also frequently been assumed to be equal to those measured at 1 bar. Estimations based on analogy have been necessary in the absence of data for many compositions and phases (53). Lacking data, it has, for example, been possible to argue either that the 410-km discontinuity is (54) or that it is not (55) associated with a change in composition. Data obtained through impulsive stimulated scattering have now confronted these issues. Examples are given in this section.

The elastic constants for olivine, orthopyroxene, and garnet have been measured to transition zone pressures at room temperature. Isotropic (Hashin-Shtrikman) average (57) bulk, K, and shear moduli have been determined (47, 48, 52). Shear and compressional velocities, determined from the isotropic moduli, are plotted as functions of pressure in Figure 8. The aluminous orthopyroxene studied by Chai et al (47) exhibited nearly linear behavior for the shear modulus and highly nonlinear behavior for the bulk modulus. At low pressure, the observed pressure derivative of the bulk modulus ($dK/dP = 8$) is almost twice typical (and often assumed) values. Above 8 GPa, dK/dP reduces to a more normal value of 4.3. In the case of olivine, the pressure dependence of the shear modulus at high pressure is distinctly nonlinear in pressure whereas the bulk modulus is nearly linear. Measured pressure dependencies are substantially at odds with prior prevailing ideas (3, 58, 59).

As indicated previously, interpretation of seismic data requires knowledge of velocities at high temperature and pressure. The techniques discussed here have

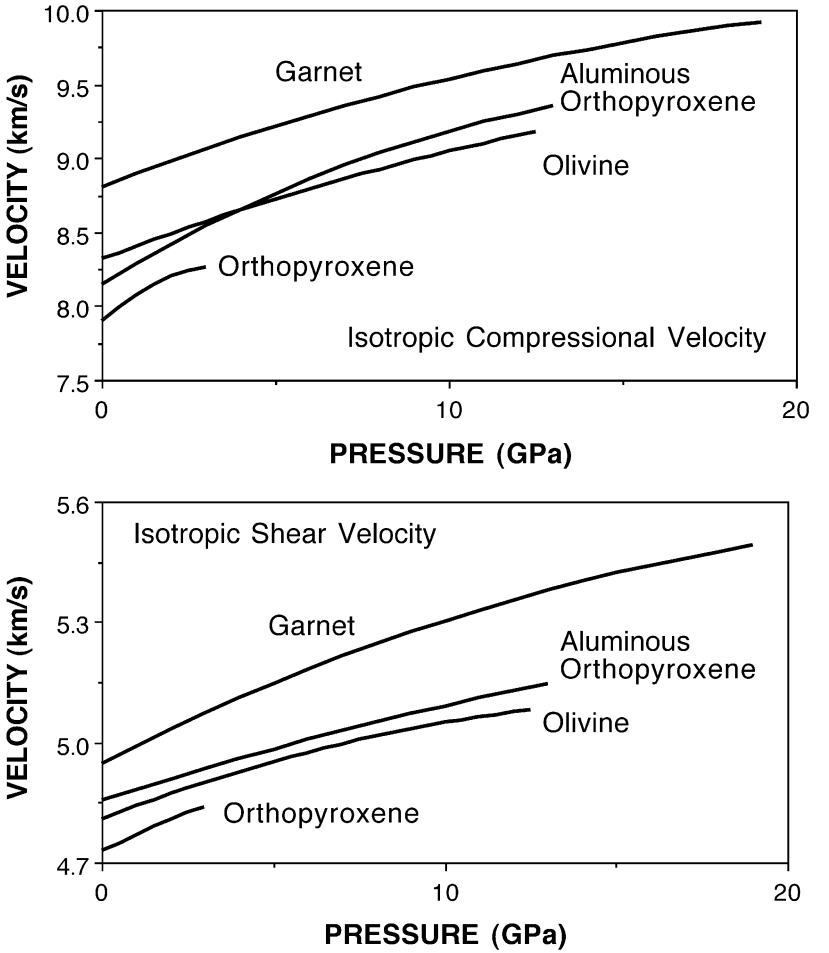

Figure 8 Isotropically averaged compressional and shear velocities in olivine, garnet, and two orthopyroxenes as functions of pressure.

been limited in temperature principally by the broadening of the R_1 ruby fluorescence at temperatures above 300°C, but mixed partial derivatives of the adiabatic moduli with respect to T and P can with care be measured. The extrapolation to mantle conditions can then be carried out on a more satisfactory basis than that possible with only temperature derivatives measured at 1 bar (60, 61). The compressional velocities in olivine at 300°C and 8 GPa are compared in Figure 9 with those calculated from room temperature elastic constants on the basis of temperature derivatives measured at ambient pressure. The temperature derivatives of the compressional elastic constants appear to be, as perhaps might be expected, ≈30% smaller in magnitude at 8 GPa than at 1 bar.

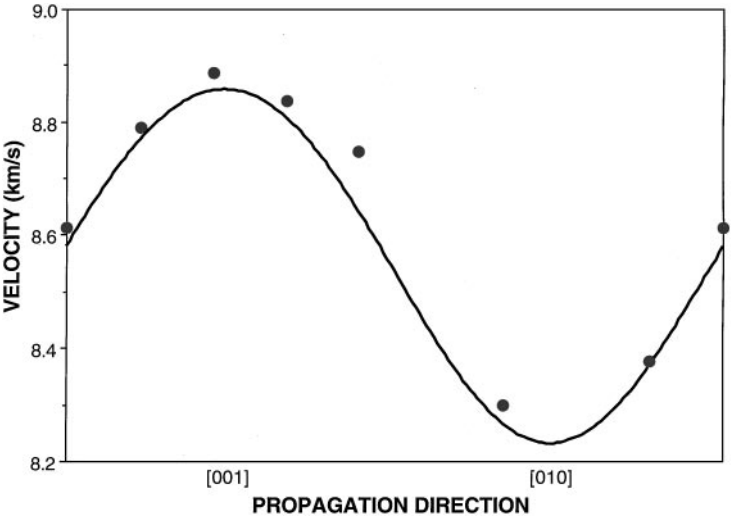

Figure 9 Measured velocities in olivine (with face-normal of *a*) at 8 GPa and 300°C (*circles*) and velocities calculated by extrapolating constants measured at 8 GPa and 25°C using temperature derivatives measured at 1 bar (*line*).

The seismic structure in the upper mantle is close to that expected for olivine, corrected to mantle temperatures (62), even though olivine may constitute only approximately 60% of the mass (38). It has been postulated that this is a consequence of the balancing of the contribution of higher-velocity garnets against that of low-velocity orthopyroxenes (58). In Figure 8, the velocities of a nonaluminous orthopyroxene $(Mg_{0.8}Fe_{0.2})SiO_3$ reported by Webb & Jackson (63) to 3 GPa are seen to be in accord with this idea. However, aluminum is an important constituent of the mantle. Except at the lowest pressures, the velocity in the aluminous orthopyroxene, having a composition not atypical of the mantle, is seen to be higher than that in olivine. The conventional interpretation of the seismic results in terms of mantle mineralogy will thus require reconsideration.

It has been postulated that the effect of composition on velocities can be predicted by one-parameter correlations based on atomic volume (53). However, as more data are obtained it has become clear that a multidimensional parameter space (*P*, *T*, and composition) must be explored (46, 64). The lateral and vertical variation in upper-mantle seismic velocities is not large (on the order of a few percent). Interpretation of small differences in seismic velocity therefore rests on an accurate knowledge of not only acoustic parameters but also the high-temperature, high-pressure chemistry of the partitioning of the elements among mineral phases. For example, the analysis of the seismic anomaly in the subcontinental mantle led Humphreys & Dueker (56) to suggest that partial melt must exist below central Colorado. However, an analysis incorporating the newer elasticity data (56a) indicates that the low velocities are a reasonable response to intrinsic temperature

derivatives augmented by compositional variation, mineral phase equilibria, and elemental partitioning among the mineral phases.

The net result of recent experiments in the diamond-anvil cell and in large-volume systems has been to reduce greatly the uncertainty associated with extrapolation of mineral properties to high pressure. The effect of temperature on the properties of the individual mineral phases can now also be more confidently anticipated. This, in turn, nominates further study of the effect of the detailed chemical composition of the mantle mineral phases on acoustic velocity as a principal requisite for progress.

Thermal Diffusivity of Minerals

The evolutionary development of a planetary body is to a considerable degree controlled by thermal transport. Overall, convection is the principal mechanism and the temperature gradient $(\partial T/\partial \mathrm{P})_s$ is implicit in the equation of state even in the case of Earth, where the mantle, although largely solid, will undergo plastic deformation over a sufficiently long timescale. However, whenever there is a barrier to mass transport, as at the Earth's surface or at the core-mantle boundary, conduction predominates. In the uppermost mantle, the geotherm (temperature as a function of depth) is deduced from surface heat flow and the thermal diffusivity of the mineral constituents. Also, the thermal diffusivity is one of the quantities that determines the Rayleigh number and thus the character of convective motion (65, 66).

There is not a large body of data on the high-pressure thermal diffusivity of crystals (17, 67–69) or fluids (70). The thermal conductivity of the Earth has often been presumed to be isotropic and nearly depth independent (65, 66, 71). However, the constituent minerals are anisotropic and preferred orientation has been reported (72) while the thermal diffusivity of olivine has been observed to increase by about 4% per GPa (17, 67).

The thermal diffusivity tensors of the principal mantle minerals have been measured (73) by impulsive stimulated scattering, in the case of olivine to 600°C. For olivine at ambient conditions, the components of D along the a, b, and c axes are, respectively, in units of $\mathrm{m^2\ s^{-1}}$ 2.16×10^{-6}, 1.25×10^{-6}, and 1.87×10^{-6}. Shear deformation in the upper mantle leads to vertical alignment of the b axis and thus to a vertical transport coefficient lower than that observed in isotropic polycrystalline samples and to a higher temperature in the upper mantle. In the case of orthopyroxene, this effect is less important, since the axis of intermediate diffusivity is preferentially aligned. Changes in the geotherm implied by the measurements of Chai et al (73) are discussed by Hearn et al (74).

The more traditional approaches to the measurement of thermal transport coefficients are often difficult at high pressure (70). Theoretical predictions are likewise limited. In principle, the thermal transport properties corresponding to a model potential are implicit in the results of a dynamical simulation. In practice, owing to the slow convergence of the energy-flux autocorrelation function, such calculations are not generally successful (75), although other approaches seem to offer promise

(75). Because values of the lattice thermal conductivity at mantle conditions are not generally available whereas the seismic velocity is directly measured, empirical or approximate theoretical connections between the velocity and the thermal conductivity would be particularly useful in a geophysical context. The sound velocities and thermal diffusivities (along with their pressure derivatives) that can be measured by impulsive stimulated scattering, in addition to their primary utility, allow the testing of connections between these quantities.

The lattice thermal conductivity κ_i associated with a single mode with group velocity c_i and mean free path λ_i is (76)

$$\kappa_i = (1/3)C_i\, c_i \lambda_i, \qquad 6.$$

where C_i is the contribution to the heat capacity made by the mode in question. Commonly, thermal resistivity associated with phonon-phonon interaction in crystals is discussed in terms of a restricted representation of the effect of vibrational anharmonicity by a Grüneisen parameter γ_i that is the value of $\mathrm{d}[\ln \nu_i]/\mathrm{d}[\ln V]$ for the *i*th lattice mode. Often the theory is further simplified by the introduction of a constant γ, set equal to the average value of γ_i.

Roufosse & Klemens (77) suggest for the phonon mean free path λ at high temperature, when Umklapp processes are the principal contributor to thermal resistivity,

$$\lambda = \frac{\sqrt{2}Mc^4}{3kT\pi(2\pi\upsilon\gamma)^2\sqrt[3]{V^o}} = \frac{\sqrt{2}Mc^2}{3kT\pi(2\pi y\gamma)^2\sqrt[3]{V^o}}, \qquad 7.$$

where M is the average atomic mass, V^o is the volume per atom, and c is the velocity of an acoustic phonon of wave vector y and frequency ν. Leibfried & Schlomann (78) have offered an approximate form that also predicts that the diffusivity scales as c^3/γ^2.

In the absence of dispersion, the pressure-dependence of the individual elastic constants serves to define an acoustic Grüneisen parameter, $\mathrm{d}[\ln c(y)]/\mathrm{d}[\ln V]$, for an acoustic phonon of wave vector y, which is directly calculable from observed quantities. In this approximation, the quantity c^3/γ^2 and thus the pressure derivative of thermal conductivity can be estimated from seismic data. In the analysis by Brown (79), lattice thermal conductivity at the base of the mantle was estimated to be roughly four times larger than in the upper mantle. In the case of the individual mantle mineral, Equations 6 and 7 give a qualitative account of the anisotropy of olivine and orthopyroxene, but they are not suitable for quantitative calculation of the elements of the diffusivity tensor (73). Here, experiment remains the only promising resource.

WATER AND AQUEOUS SOLUTIONS

General Considerations

At ambient pressure, impulsive stimulated scattering has been applied to the study of relaxation dynamics in fluids extending over more than two decades of

frequency (80). The geometry of the diamond-anvil cell in conjunction with the requirement that there be many cycles of the grating contained in the small lateral dimensions of the sample has restricted measurements in fluids to frequencies between a few hundred megahertz and 1–2 GHz. In many simple fluids and solutions at ambient or moderate pressure, the absence of significant dispersion or acoustic absorption indicates that frequencies in this range lie well below the relaxation frequency ($f_R = 2\pi\tau^{-1}$) associated with perturbation of structural or chemical equilibria. In this regime, the direct interpretation of acoustic velocities in terms of an equation of state is possible. At somewhat higher pressures or lower temperatures, analysis of acoustic dispersion and absorption provides information about viscoelastic behavior (81, 82) as well as a route to the density, P, T relations.

The requirement that the value of $\gamma r/c$ (here γ is the temporal damping coefficient, r is the radius of the probe beam, and c is the velocity of sound) be not much less than 1 sets a limit to the detectable absorption. At less than 200°C in the diamond-anvil cell, the true acoustic absorption in water and aqueous Na_2SO_4 is barely measurable and no dispersion is observed. At higher temperature and moderate pressure, where the equilibrium constants are more favorable and the volume change of the reaction is large, simple feasibility calculations indicate that the frequency dependence of γ and the velocity might be employed in the investigation of ion-pairing kinetics and equilibria. Either slow structural relaxation in water or slow relaxation of ion-pairing equilibrium would, however, introduce error in the deduction of the equation of state from the velocities. In the concentrated solutions so far investigated, the relaxation frequencies of simple diffusion controlled reactions are expected to be larger than the experimental frequencies, and it seems likely that in this case an equilibrium velocity is measured.

At temperatures where the density and heat capacity of a fluid are known for at least one pressure, the equation of state at fixed composition can be determined from the pressure dependence of the low-frequency limit of the velocity of sound by recursive integration of

$$\left(\frac{\partial\rho}{\partial P}\right)_T = \frac{1}{c^2} + \frac{T\alpha^2}{c_P} \quad \text{and} \quad \left(\frac{\partial c_P}{\partial P}\right)_T = -T\left(\frac{\partial^2 v_{sp}}{\partial T^2}\right)_P, \qquad 8.$$

where ρ is the density, α the coefficient of thermal expansion, c_P the specific heat, and v_{sp} the specific volume. To deduce v_{sp} at higher temperatures, the Gibbs free energy per gram at each composition can be expanded around any chosen temperature T^o in the form

$$G_{sp} = \sum_{ij} A_{ij} P^i (T - T^o)^j, \qquad 9.$$

appropriately differentiated, and the coefficients adjusted to match the P, v_{sp}, T relations as derived at lower temperature from Equation 8, from the measured pressure dependence and temperature dependence of the heat capacity where

known, and from the measured velocity of sound at high temperature and pressure. The specific volume is then given by

$$v_{sp} = \left(\frac{\partial G_{sp}}{\partial P}\right)_T. \qquad 10.$$

The Equation of State of Water

The equation of state of water at moderate temperature has been determined by conventional methods (83) from the liquid-vapor coexistence curve to 1 GPa. Thermally stimulated Brillouin scattering has extended these results to 3.5 GPa (30). In the common range of pressure, the agreement between the two methods is excellent. Empirical equations of state and the results of molecular dynamics simulations are compared with experiment in Figure 10. At higher pressures, the 58-term equation of Saul & Wagner (84), which is largely based on data below 1 GPa but is also constrained to match the shock wave Hugoniot (85–87), consistently gives the best description of the experimental densities. The deviation is less than 0.1% everywhere below 2.5 GPa, and the largest discrepancy is 0.3% at 3.5 GPa, which corresponds to an error in free energy of ≈175 J mol^{-1}. The National Bureau of Standards steam tables are less satisfactory (83).

The T1P4P potential (88, 89) supposes a rigid gas-phase molecular geometry and represents the interaction of two water molecules by a Lennard-Jones 6–12 term centered on the oxygen and the coulomb energy of positive charges of 0.52e on each of the H atoms with a compensating negative charge 0.15 Å from the oxygen atom on the C_2 axis of the water molecule. Above 1 GPa, the densities at 100° and 200°C calculated from this potential are no more than 0.8% above experiment (Figure 10, *B&W*). An extrapolation to 10 GPa of the nearly uniform 0.8% difference between the experimental and calculated specific volumes would translate to a difference in chemical potential of approximately 1 kJ mol^{-1}.

The stimulated Brillouin experiments yield a coefficient of thermal expansion that, at high temperature and pressure, increases monotonically with increasing temperature and decreases monotonically with increasing pressure and values of the specific heat that decrease uniformly with increasing pressure. In this respect the simulation based on the T1P4P potential is at 200°C closer to experiment than the predictions of any of the empirical equations of state. Approximating intermolecular interactions in water by those of a monatomic species with exponential repulsion and r^{-6} attraction (90) (Figure 10, *B&S*) is less successful.

The reactions of water in the crust and upper mantle involve temperatures of up to 1500°C and pressures of more than 10 GPa (89, 91). Although the agreement between T1P4P-based simulations and experimental densities does improve with increasing pressure, Figure 10 indicates that as temperatures increase, the portion of the isotherm poorly described by the simulations also increases. The present experiments might constitute an intuitive basis for minor refinement of TIP4P, in that a small adjustment to the Lennard-Jones σ would procure the slight increase

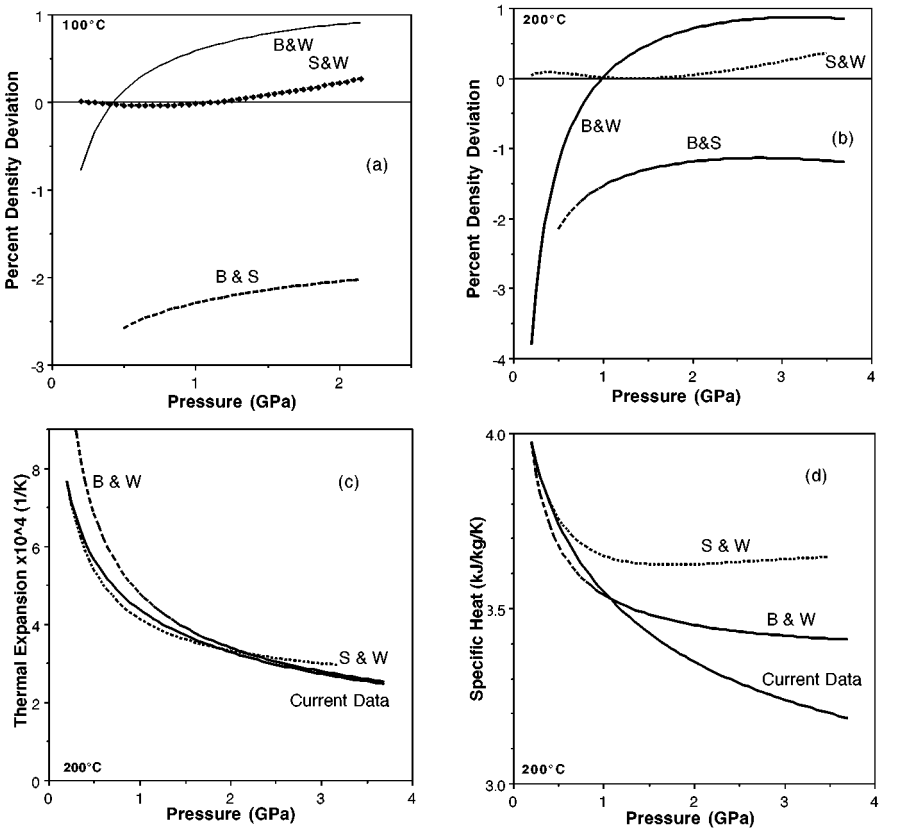

Figure 10 Deviations of equations of state for water from that derived from thermally stimulated Brillouin spectroscopy (30). Densities are compared at 100°C (*a*) and 200°C (*b*) with the most successful empirical equation of state (84) (*S&W*), the result of molecular dynamics simulations based on the T1P4P potential (89) (*B&W*), and a spherically symmetric exponential-6 potential (106) (*B&S*). The coefficient of thermal volume expansion (*c*) and the specific heat (*d*) are also compared at 200°C with the results of simulation.

in specific volume necessary to produce agreement with the measured density at high pressure (at the price of slightly greater deviations nearer ambient conditions). However, a more fundamental revision of the potential would be required before the moderate temperature isotherms were described with sufficient accuracy to justify an application to conditions appropriate to the mantle.

Incidental to principal objects of these studies, thermally stimulated Brillouin spectroscopy in conjunction with the results of conventional Brillouin spectroscopy at large scattering angles (where the product of acoustic velocity and the index of refraction, rather than the velocity itself, is directly measured) (92) also offers a

route to determination of the indices of refraction of fluids at higher pressures than are accessible by conventional techniques (93, 94).

Ionic Solutions

Equations 8–10 allow the deduction of the specific volume of a solution at high temperature and pressure from acoustic data and values at ambient or moderate pressure. If f is the fraction by weight of solute, the quantity $(v_{sp}/1 - f)$ is the volume of the solution that contains 1 g of solvent. The number of moles (n) of a solute with formula weight w in this volume is given by $n = f/(1 - f)w$.

Introducing the definition $y = [v_{sp}/(1 - f)] - v^{o}$, where v^{o} is the specific volume of the pure solvent, the partial molal volume of the solute species is $V = (\partial y/\partial n)_{TP}$. The pressure dependence of the total chemical potential, standard chemical potential, and mean activity coefficients of the solute species at high pressure can be calculated from measurements of y as a function of concentration, temperature, and pressure by

$$\mu(PTn) = \mu(P_{ref}Tn) + \int_{P_{ref}}^{P} \frac{\partial y}{\partial n} dP$$

$$\mu^{o}(\mathrm{PT}) = \mu^{o}(P_{ref}T) + \int_{P_{ref}}^{P} V^{o} dP \qquad 11.$$

$$3 \ln\left(\frac{\gamma(PTn)}{\gamma(P_{ref}Tn)}\right) = \frac{1}{RT} \int_{P_{ref}}^{P} \frac{\partial V_{excess}}{\partial n} dP, \qquad 12.$$

where V^{o} is the partial molal volume at infinite dilution $V_{excess} = V - V^{o}$ and the factor of 3 is appropriate to sodium sulfate.

The result of the application of this procedure to 0.5-molal aqueous sodium sulfate at 100°C is given in Figure 11, where the changes in the total chemical potential, the standard chemical potential, and the excess chemical potential of the solute are plotted as functions of pressure to 1.5 GPa (94a). At pressures up to 0.5 GPa, where the dielectric constant of water is known, the effect of pressure on the excess chemical potential in the Debye-Hückel approximation (95) can also be calculated. The portion of the pressure dependence of the excess chemical potential not accounted for by the Debye-Hückel expression is also displayed in Figure 11. Up to 0.5 GPa, the Debye-Hückel theory, in conjunction with the parameterization of the pressure dependence of the dielectric constant by Bradley & Pitzer (96), is seen to give a perhaps surprisingly good account of the change in the excess potential in these fairly concentrated solutions.

In Figure 11, the largest part of the pressure dependence of μ is the change in the standard potential, that is $\int V^{o} dP$. The Born model of the electrostatic free energy of a spherical ion in a dielectric continuum, specialized to the case of an incompressible solute, predicts that V^{o} is the resultant of a temperature- and

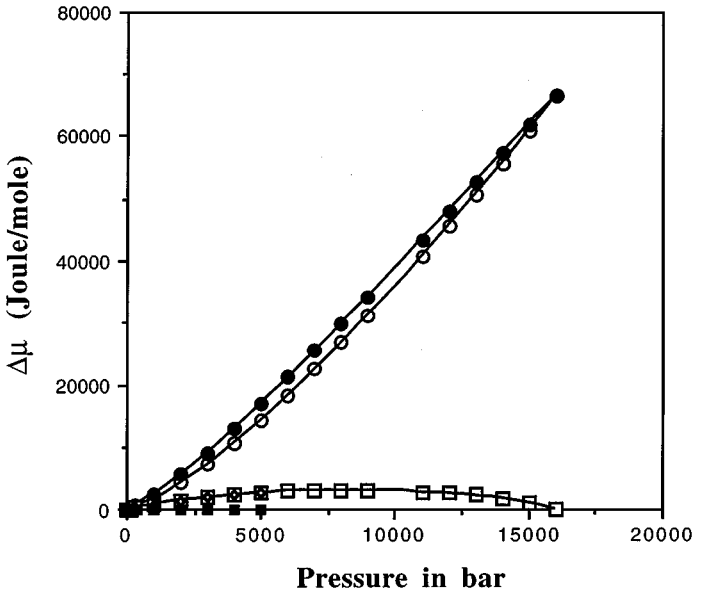

Figure 11 The pressure dependence of the chemical potential of Na_2SO_4 in 0.5-molal aqueous solution at 100°C. (*Solid circles*) The change in the total chemical potential from its value at 1 bar; (*open circles*) the change in the standard potential; (*open squares*) the change in the excess chemical potential; and (*solid squares*) the portion of the pressure dependence of the excess chemical potential not accounted for by the Debye-Huckel free energy.

pressure-independent hard sphere volume peculiar to each solute species and a negative electrostrictive contribution proportional to the value of $(\partial D^{-1}/\partial P)_T$ in the solvent (here D is the dielectric constant). The molal volume of the solute in aqueous sodium sulphate is plotted versus the pressure derivative of $(1/D^2)\partial D/\partial P$ in Figure 12. The points span the temperature range from 20.4° to 250°C. The pressure varies from 1 to 280 bar. A naive electrostatic model is seen to be successful in this limited regime of pressure appropriate, for example, to the description of processes at mid-ocean ridges. At higher pressures (Figure 13), the electrostrictive term is no longer dominant and the pressure dependence of V^o is correspondingly more complex.

If the excitation pulses are selected from the 1064-nm output of a Nd-YAG laser, the thermoacoustic signal derived from absorption by the overtone of the OH stretching mode should be strong in any aqueous solution. Except in the neighborhood of the density maximum, any aqueous solution should be amenable to study.

The interaction of sea water with oceanic crust at spreading centers, which controls the composition and evolution of the oceanic crust and strongly affects

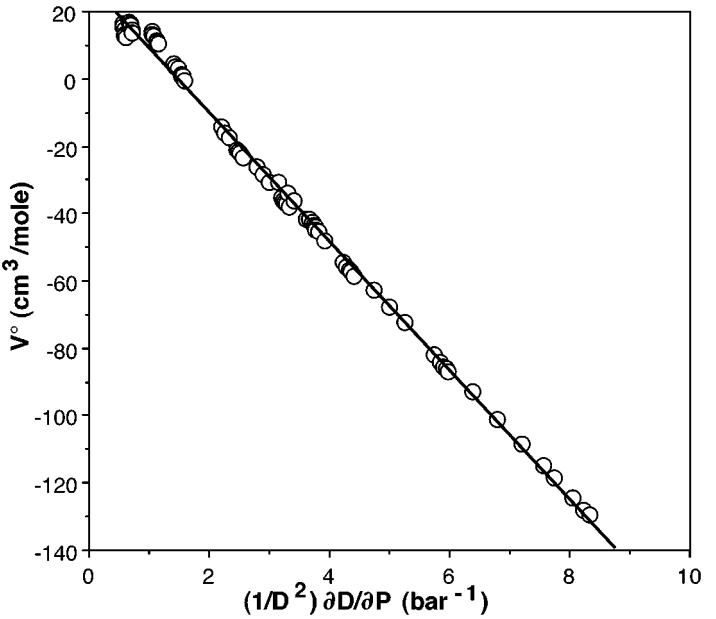

Figure 12 The molal volume of Na_2SO_4 in aqueous solution at infinite dilution versus $(1/D^2)\partial D/\partial P$. The data span the temperature range from 20.4° to 250°C and extend from 1 to 280 bar. (*Lower right*) Points represent data at 250°C; (*upper left*) points represent data at 20.4°C.

chemical properties of the oceans, may involve temperatures as high as 500°C. The experimental limits in water have been set by dissolution of the ruby pressure standard in a diamond-anvil cell or the sapphire windows of a conventional cell. This process is slow below 200°C and rapid above 300°C. To the extent that the results in Figures 11 and 12 prove to be general, the pressure dependence of the standard chemical potentials and activities at the higher temperatures but modest pressures encountered near mid-ocean spreading centers are to a reasonable approximation implicit in the pressure and temperature dependence of the dielectric constant of water.

SIMPLE MATERIALS

Force Models

The complexity of the crystal structures of the mantle minerals makes the microscopic interpretation of macroscopic properties difficult. In addition, these crystals are relatively incompressible, and the large variation in density that is of interest in

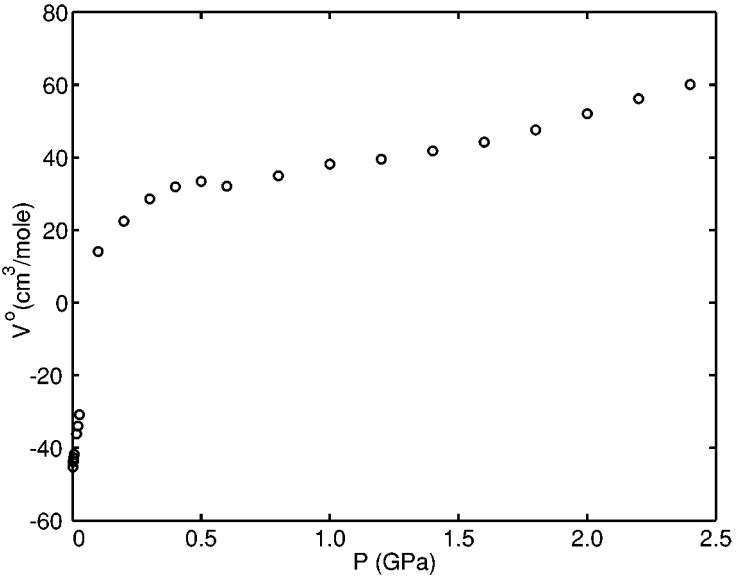

Figure 13 The partial molal volume of Na_2SO_4 in aqueous solution at infinite dilution versus pressure at 200°C. The rapid initial increase in V^o reflects the decrease in the electrostrictive effect as the pressure is increased. The values at high pressure are, however, significantly larger than a hard-sphere volume derived from that data in Figure 12.

the theory of intermolecular forces is not easily achieved. β-Oxygen, which is both crystallographically simple and highly compressible, is a logical candidate for the analysis of macroscopic tensorial properties in terms of intermolecular forces. At room temperature, β-oxygen forms from the melt at 5.9 GPa and remains stable until 9.6 GPa, at which pressure it transforms to the δ phase (97, 100, 101). The crystal (point group D_{3d}) has six independent elastic constants, which have been measured as functions of pressure to 9.5 GPa (98). The thermal diffusivity tensor, D, referred to a Cartesian coordinate system with z along the threefold axis, is diagonal with $D_{xx} = D_{yy} \neq D_{zz}$. The elements of D and their pressure derivatives have been measured (69) by the techniques outlined in the experiment section.

The structure (101, 108) is depicted schematically in Figure 14. There is one molecule per primitive rhombohedral cell, with the molecules aligned parallel to the threefold axis. The nearest nonbonded molecular neighbors are approximately cubic-close-packed. In addition to the covalently bonded 0′, the atom designated by 0 in Figure 14 has three nearest nonbonded neighbors (7′ and equivalent atoms), six second nearest neighbors (represented by atom 12), and six third nearest neighbors (i.e. 12′).

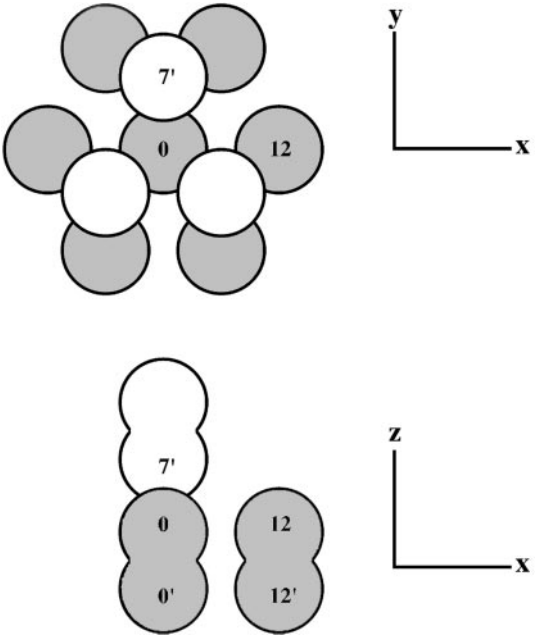

Figure 14 The crystal structure of β-oxygen viewed along and normal to the threefold axis. (*Unshaded circles, upper panel*) Above the plane of the shaded atoms.

The program of quasiharmonic lattice dynamics (102) is to expand U, the potential energy of the crystal in terms of the displacement of each atom from its equilibrium position in a homogeneously strained lattice. If $u_\alpha(i)$ represents the αth Cartesian component of the displacement of the ith atom, the elements of the force constant matrix $\Phi(ij)$ specifying the interaction of atoms i and j are defined by

$$\Phi_{\alpha\beta}(ij) = \frac{\partial^2 U}{\partial u_\alpha(i)\partial u_\beta(j)}. \qquad 13.$$

The substitution of traveling wave solutions into the harmonic equations of motion generate, for a crystal with n atoms in the primitive unit cell, a $3n \times 3n$ secular equation that expresses the frequencies of the normal modes as a function of the wave vector y and the force constants. Solution of the secular equation at values of y consonant with the cyclic boundary conditions generates the normal frequencies of vibration of any particular model of a cyclically bounded crystal. The long-wave limit of the lattice dynamical secular equation expresses the fundamental infrared and Raman modes and the elastic constants of the crystal in terms of the force constants. The force constants between an atom and a set of near neighbors can

then be evaluated from knowledge of the measured elastic properties and optical spectra.

The approach (103, 104) taken by Abramson et al (69, 98) is to write each Φ in the most general form consistent with the point symmetry of the crystal, rotational and translational invariance, and the vanishing of anisotropic stress. This avoids any assumption about the form of the repulsive potential. However, inherent in such an approach is the presumption that the repulsive interactions are sufficiently short range so that forces between a small set of nearest neighbors suffices.

It is shown (98) that no reasonable central force model or a model based on central forces augmented by interaction between axial quadrupoles (105) can account for the relative magnitudes of the elastic constants of β-oxygen. Both a good account of the acoustic data and adequate reproduction of the libron frequency (which is extrapolated from lower pressures and temperatures) have been obtained from models in which the elements of Φ that would be zero in the central force approximation are comparable in magnitude to the central forces terms.

Although it is not possible to reproduce properly the elastic tensor without noncentral terms, the structure of crystalline oxygen has been rationalized (105) up to several gigapascal and, separately, up to a temperature of 30 K through use of a potential based on central forces (with the addition of a small quadrupole term). This potential reproduces both cell parameters and first-order phase changes and may therefore be considered successful as a description of the *PVT* properties of oxygen. Thus it is seen that a potential that correctly predicts the density may not be reliable when it is called on in calculations of the elastic constants and, probably, other properties.

Fluid Oxygen

At 25°C, molecular oxygen remains a supercritical fluid up to the unusually high pressure of 5.8 GPa, and at 200°C up to 10.5 GPa. As seen in Figure 15, sound velocities have been measured in this range (105a). Even without further interpretation, these data afford a useful standard for the validation of calculational methods used to predict the properties of dense fluids. For example, the *PVT* surface of oxygen has been modeled based on a spherically symmetric, exponential-6 potential (106) for pressures in excess of 0.5 GPa and temperatures over 400 K. Sound velocities are implicit in the results, given an initial value of the heat capacity at low pressure. The results of the model (also shown in Figure 15) are uniformly low, from ~20% at 0.5 GPa to ~2% at 11 GPa; whether this indicates a crossing or convergence of the results has not been determined.

The thermal diffusivity of this dense fluid has also been measured (Figure 16), and through use of the heat capacity calculated from the acoustic equation of state (Equation 8), the thermal conductivity can then be estimated. Simple expressions have been proposed for the thermal diffusivity of dense diatomic fluids.

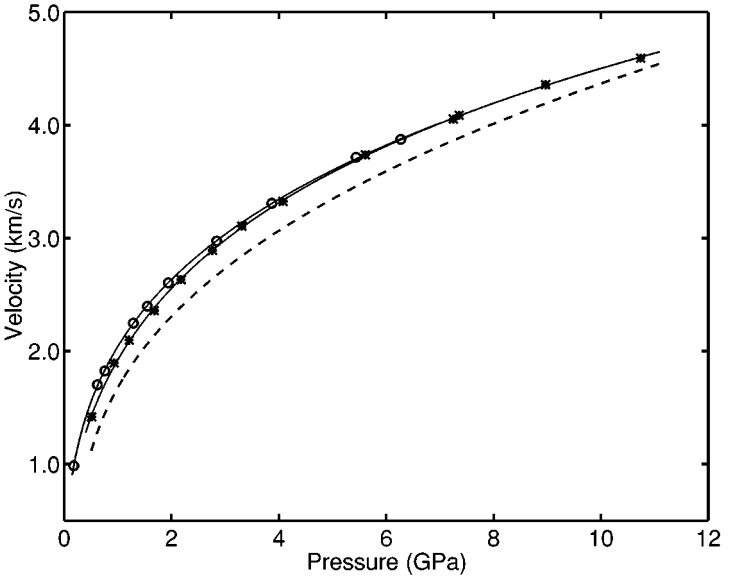

Figure 15 Velocities of sound in supercritical, fluid oxygen are shown up to the melting pressures at 30°C (*circles*) and 200°C (*asterisks*). (*Solid lines*) Fits through the experimental data; (*dashed line*) calculations based on an exponential-6 potential for a temperature of 200°C (106).

Stevenson & Salpeter in their analysis (107) of the structure of the giant planets use

$$D = c\sigma\sqrt{\frac{kT}{M}}, \qquad 14.$$

where σ is a hard-sphere diameter, c a correction factor of order unity, and M the molecular mass. It is seen in Figure 16 (107a) that, as required by Equation 14, the diffusivity of dense, supercritical oxygen is approximately independent of the pressure (from 1 to 5 GPa). With $c = 1$ and a hard-sphere diameter (2.7 Å) derived from the nearest-neighbor distance in the close-packed crystal (101, 108), the measured value of D is, however, greater than that predicted by Equation 14 by a factor of 2.5. As in the case of water, there is an experimental basis for the refinement of potentials based on thermodynamic and, in this case, dynamic constraints.

VISCOELASTIC BEHAVIOR AND RELAXATION

The records for methanol given in Figure 17 illustrate both some interpretative complications and the additional dynamic information that can be derived from thermally stimulated Brillouin scattering. At low pressures (Figure 17*c*), where

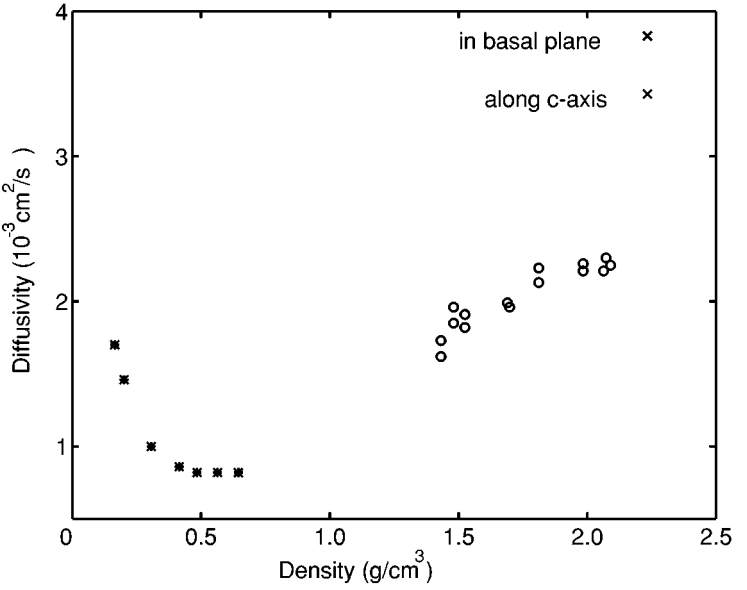

Figure 16 Thermal diffusivities in fluid oxygen at 30°C are plotted against density. (*Asterisks*) Data taken at pressures from 12 to 64 MPa (111); (*circles*) data taken between 1 and 5 GPa, with densities derived from measured sound velocities; (*crosses*) thermal diffusivities in solid β-oxygen (at 6.1 GPa).

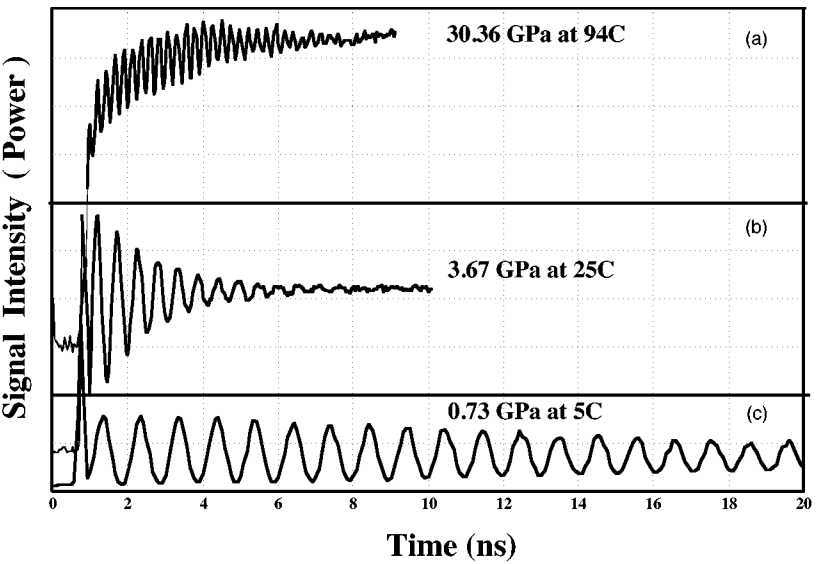

Figure 17 Representative time domain records for scattering from methanol at frequencies above (*a*), comparable with (*b*), and below (*c*) the relaxation frequency.

structural relaxation is rapid compared with the period of the ultrasonic wave, there is no damping, although there is an apparent decay of the signal as the acoustic waves travel beyond the area illuminated by the probe. The equation of state may be directly deduced from the velocity in this regime. As the pressure is raised, structural relaxation slows until the characteristic time is comparable with the acoustic period (~100 ps). In this regime (Figure 17*b*), there is strong damping. The low-frequency limit of the velocity appropriate for the deduction of the equation of state as well as the structural relaxation time can be determined by varying the angle of intersection of the excitation pulses and, thus, observing the frequency dependence of the acoustic velocity and absorption. At still higher pressures, the damping per cycle diminishes as the structural relaxation time increases well beyond the acoustic period (Figure 17*a*) and is replaced by observation (in the time domain) of a slow structural relaxation extending over several nanoseconds (the "Mountain mode"). In this regime, the equation of state cannot be derived from the acoustic data. At the highest pressure, the velocity is high enough so that the acoustic period is not long compared with the laser pulse duration, and the excitation process is consequently less efficient; however, a good signal-to-noise ratio is maintained.

In a medium with a single relaxation process with characteristic time τ, the velocity of sound c at circular frequency ω may be expressed as (81)

$$\begin{aligned} c^2 &= \frac{K_o}{\rho}\left(1 + \frac{K_\infty - K_o + \frac{4}{3}G_\infty}{K_o}\frac{(\omega\tau)^2}{1+(\omega\tau)^2}\right) \\ &= c^{o^2}\left(1 + \frac{K_\infty - K_o + \frac{4}{3}G_\infty}{K_o}\frac{(\omega\tau)^2}{1+(\omega\tau)^2}\right) \\ &= c^{o^2}\left(1 + A\frac{(\omega\tau)^2}{1+(\omega\tau)^2}\right). \end{aligned} \quad 15.$$

With the same assumptions, the frequency dependence of the absorption per cycle, γ/f, is

$$\frac{\gamma}{f}\left(\frac{c}{c^o}\right)^2 = \frac{A}{2}\left(\frac{\omega^2\tau}{1+(\omega\tau)^2}\right), \quad 16.$$

where c^o is the low-frequency velocity, K and K_o, respectively, are the high- and low-frequency limits of the bulk modulus, and G_∞ is the high-frequency limit of the shear modulus. The low-frequency viscosity is $\eta^o = G_\infty\tau$.

The absorption per wavelength in methanol is plotted in Figure 18 as a function of pressure at several temperatures and two wavelengths. In the range of pressures in which the maximum in γ/f at $\omega\tau = 2\pi f\tau \approx 1$ is accessible, the determination of τ from Equations 15 and 16 is formally straightforward, and the temperature and pressure dependence of the relaxation time can be explored. However, the peak in γ/f defined by Equation 16 is broad, and the lack of resolved structure

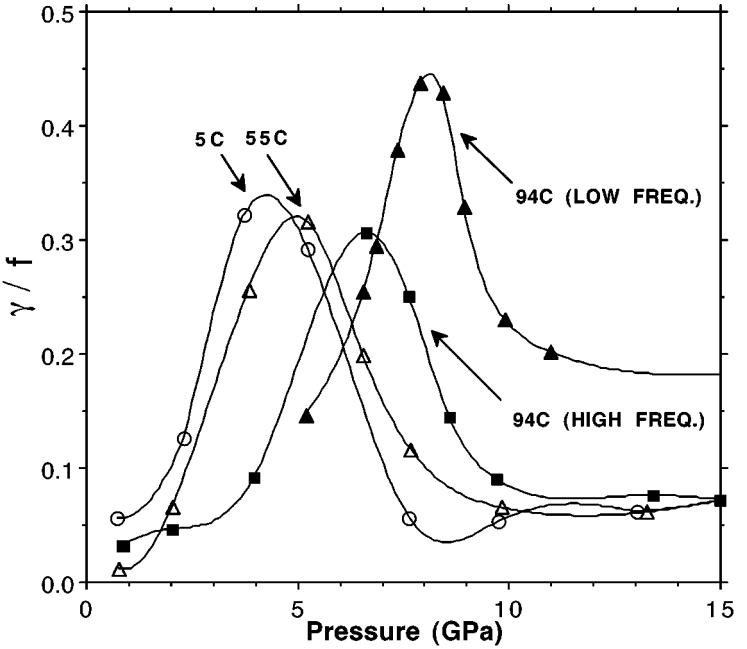

Figure 18 The acoustic absorption per wavelength in methanol at wavelengths of 7.63 μm and 2.37 μm as a function of pressure and temperature. (*Solid triangles*) Data at 7.63 μm and 94°C. The frequency at the absorption maximum is 0.8 GHz, corresponding to a relaxation time of 0.2 ns. (*Open circles, open triangles, solid squares*) Results at 2.37 nm and 5°C, 55°C, and 94°C, respectively. The relaxation times corresponding to the peaks in damping are respectively 85 ps, 80 ps, and 69 ps.

in Figure 18 cannot be taken as indicative of a single characteristic time. The frequency and absorption at the peak do serve to define an average relaxation time and amplitude.

Alternatively, for a single process, when the relaxation frequency lies within the experimentally accessible range of frequencies, c^o, K_o, the relaxation time, and the relaxation amplitude at fixed temperature and pressure can be obtained, as in Figure 19, directly from the velocity dispersion by means of Equation 15. However, measurement of only dispersion or absorption, even in the context of a single characteristic time, provides no basis for the separation of the relaxational contributions of the bulk modulus from those of the shear viscosity.

Adaptation of the ingenious methods developed by Herbst et al (109) for measurement of viscosity in the diamond-anvil cell to work at elevated temperature offers, in conjunction with the methods discussed here, one possible approach to proceeding beyond a deduction of the equilibrium bulk modulus and the equation

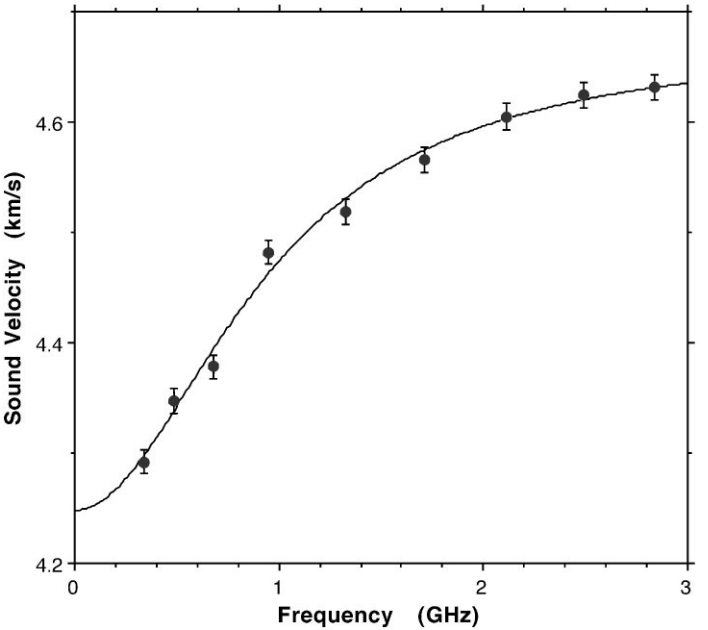

Figure 19 The velocity of sound as a function of frequency in methanol at 3.7 GPa and 25°C. (*Solid curve*) A single relaxation with $c_0 = 4.247$ km s^{-1}, $c_\infty = 4.673$ km s^{-1}, and a relaxation frequency of 0.97 GHz.

of state to a more complete description of the viscoelastic behavior of fluids at high temperature and pressure.

SUMMARY

The development of conventional ultrasonic techniques in large-volume high-pressure systems, of experimental advances in frequency-domain Brillouin spectroscopy, and of applications of time-domain optical spectroscopy are together providing a firmer experimental foundation for the physical and chemical interpretation of seismic structure and hence a more reliable picture of the structure and dynamics of Earth's mantle. Both thermodynamic and transport properties can be studied at pressures consonant with the mantle and at moderately high temperature. The equations of state of a few simple fluids, of water, of oxygen, and of methanol have been extended toward significantly higher densities. In the case of methanol, the dynamics of structural relaxation have also proven amenable to study. These data provide a basis for the refinement of intermolecular potentials and a test at intermediate density and temperature of methods that might be applied to experimentally inaccessible conditions. In the case of water and oxygen, it is argued that some commonly used potentials are inadequate.

LITERATURE CITED

1. Dziewonski AM, Anderson DL. 1981. *Phys. Earth Planet Inter.* 25:297–356
2. Grand SP, van der Hilst RD, Widiyantoro S. 1997. *Geol. Soc. Am. Today* 7:1–7
3. Agee CB. 1998. See Ref. 112, pp. 165–203
4. Bina CR. 1998. See Ref. 112, pp. 205–39
5. Liebermann RC, Li B. 1998. See Ref. 112, pp. 459–92
6. Zha CS, Duffy TS, Downs RT, Mao HK, Hemley RJ. 1996. *J. Geophys. Res.* 101: 17535–45
7. Stevenson DJ. 1982. *Annu. Rev. Earth Planet. Sci.* 10:257
8. Stoneham AM, Harding JH. 1986. *Annu. Rev. Phys. Chem.* 37:53
9. Axilrod BM, Teller E. 1943. *J. Chem. Phys.* 11:299–300
10. Bulski M. 1991. See Ref. 113, pp. 353–88
11. Barker JA. 1991. See Ref. 113, pp. 341–51
12. Barker JA. 1991. See Ref. 113, pp. 331–39
13. Fayer MD. 1982. *Annu. Rev. Phys. Chem.* 33:63–87
14. Fayer MD. 1986. *IEEE J. Quantum Electron.* 22:1437–52
15. Yan YX, Cheng LT, Nelson KA. 1988. In *Advances in Non-Linear Spectroscopy*, ed. RJH Clark, RE Hester, 15:299–355. New York: Wiley
16. Brown JM, Slutsky LJ, Nelson KA, Cheng L-T. 1989. *J. Geophys. Res.* 94:9485–92
17. Zaug J, Abramson EH, Brown JM, Slutsky LJ. 1992. In *High Pressure Research; Applications to Earth and Planetary Sciences*, ed. Y Syono, M Manghnani, pp. 157–66. Washington, DC: Am. Geophys. Union
18. Rogers JA, Nelson KA. 1994. *J. Appl. Phys.* 75:1534–56
19. Rogers JA, Dhar L, Nelson KA. 1994. *Appl. Phys. Lett.* 65:312
20. Maznev AA, Nelson KA, Rogers JA. 1998. *Opt. Lett.* 23:1319–21
21. Barnett DM, Lothe J, Gayazza SD, Musgrave MJP. 1985. *Proc. R. Soc. London Ser. A* 402:153
22. Morocha AK, Shermergor TD, Yashina AN. 1975. *Sov. Phys. Acoust.* 20:524–27
23. Piermarini GJ, Block S, Barnett JD, Forman RA. 1975. *J. Appl. Phys.* 46:2774–80
24. Mao HK, Bell PM, Shaner JW, Steinberg DJ. 1978. *J. Appl. Phys.* 49:3276–83
25. Mao HK, Xu J, Bell PM. 1986. *J. Geophys. Res.* 91:4673–76
26. Wunder SL, Schoen PE. 1981. *J. Appl. Phys.* 52:3772–75
27. Bridgman PW. 1942. *Proc. Am. Acad. Arts Sci.* 74:399–424
28. Vedam R, Holton G. 1968. *J. Acoust. Soc. Am.* 43:108–16
29. Grindley T, Lind JE Jr. 1971. *J. Chem. Phys.* 54:3983–89
30. Wiryana S, Slutsky LJ, Brown JM. 1998. *Earth Planet. Sci. Lett.* 163:1–4
31. Qi B, Brown JM, Sato-Sorensen Y. 1990. *J. Appl. Phys.* 68:5357–59
32. Hess NJ, Schiferl D. 1992. *J. Appl. Phys.* 71:2082–86
33. Yuechao Z, Barvosa C-W, Theiss SD, Mitha S, Aziz MJ, Schiferl D. 1998. *J. Appl. Phys.* 84:4049–59
34. Lacam A, Genotelle M, Chateau C. 1986. *CR Acad. Sci. Ser. II* 303:547–52
35. Lacam A, Chateau C. 1989. *J. Appl. Phys.* 66:366–72
36. Schiferl D, Nicol M, Zaug JM, Sharma SK, Cooney TF, et al. 1997. *J. Appl. Phys.* 82:3256–65
37. McDonough WF, Sun S-S. 1995. *Chem. Geol.* 120:223–53
38. McDonough WF, Rudnick RL. 1998. See Ref. 112, pp. 139–64
39. Kennett BLN, Engdahl ER, Buland R. 1995. *Geophys. J. Int.* 122:108–24
40. Gasparik T. 1990. *J. Geophys. Res.* 95: 15751–69

41. Kesson SE, Fitz Gerald JD. 1992. *Earth Planet. Sci. Lett.* 111:229–40
42. Fei Y, Wang Y, Finger LW. 1996. *J. Geophys. Res.* 101:11525–30
43. McCammon C. 1997. *Nature* 387:694–96
44. Brown JM, Shankland TJ. 1981. *Geophys. J. R. Astron. Soc.* 66:579–96
45. Watt JP, Davies GF, O'Connell RJ. 1976. *Rev. Geophys. Space Phys.* 14:541–63
46. Collins MD, Brown JM. 1998. *Phys. Chem. Min.* 26:7–13
46a. Nye JF. 1992. *Physical Properties of Crystals*. Oxford, UK: Clarendon
47. Chai M, Brown JM, Slutsky LJ. 1997. *J. Geophys. Res.* 102:14779–85
48. Abramson EH, Brown JM, Slutsky LJ, Zaug J. 1997. *J. Geophys. Res.* 102: 12253–63
49. Kudoh Y, Takeuchi Y. 1985. *Z. Kristall.* 171:291–302
50. Brodholt J, Patel A, Refson K. 1996. *Am. Mineral.* 81:257–60
51. Zha CS, Duffy TS, Downs RT, Mao HK, Hemley RJ. 1998. *Earth Planet. Sci. Lett.* 159:25–33
52. Chai M, Brown JM, Slutsky LJ. 1997. *Geophys. Res. Lett.* 24:523–26
53. Anderson DL. 1989. *Theory of the Earth*. Boston: Blackwell
54. Anderson DL, Bass JD. 1984. *Geophys. Res. Lett.* 11:637–40
55. Weidner DJ, Ito E. 1987. In *High Pressure Research in Mineral Physics*, ed. MH Manghanani, Y Syono, pp. 439–46. Tokyo: Terra Sci.
56. Humphreys ED, Dueker KG. 1994. *J. Geophys. Res.* 99:9635–50
56a. Brown JM. Manuscript in preparation
57. Watt JP, Peselnick L. 1980. *J. Appl. Phys.* 51:1525–31
58. Duffy TS, Anderson DL. 1989. *J. Geophys. Res.* 94:1895–912
59. Helffrich GR, Stein S, Wood BJ. 1989. *J. Geophys. Res.* 94:753–63
60. Isaak DG, Anderson OL, Goto T, Suzuki I. 1989. *J. Geophys. Res.* 94:5895–906
61. Isaak DG. 1992. *J. Geophys. Res.* 97: 1871–85
62. Zaug JM, Abramson EH, Brown JM, Slutsky LJ. 1993. *Science* 260:1487–89
63. Webb SL, Jackson I. 1993. *Eur. J. Mineral.* 5:1111–19
64. Gwanmesia GD, Chen GL, Liebermann RC. 1998. *Geophys. Res. Lett.* 25:4553–56
65. Spohn T, Schubert G. 1982. *J. Geophys. Res.* 87:4682–96
66. Christensen UR. 1989. *Philos. Trans. R. Soc. London Ser. A* 328:417–24
67. Fujisawa H, Fujii N, Mizutani H, Kanamori H, Akimoto S. 1968. *J. Geophys. Res.* 73:4727–33
68. Schärmeli GH. 1982. In *High-Pressure Researches in Geoscience*, ed. W Schreyer, pp. 349–73. Stuttgart, Germany: Schweizerbart'sche
69. Abramson EH, Slutsky LJ, Brown JM. 1996. *J. Chem. Phys.* 104:5424–28
70. Ross RG, Andersson P, Sundqvist B, Backstrom G. 1984. *Rep. Prog. Phys.* 47: 1347–402
71. Kieffer SW. 1976. *J. Geophys. Res.* 81: 3025–30
72. Babuska V, Cara M. 1991. *Seismic Anisotropy in the Earth*. Dordrecht, The Netherlands: Kluwer Academic
73. Chai M, Brown JM, Slutsky LJ. 1996. *Phys. Chem. Min.* 23:470–75
74. Hearn EH, Humphreys ED, Mu C, Brown JM. 1997. *J. Geophys. Res.* 102:11943–56
75. Müller-Plathe F. 1997. *J. Chem. Phys.* 106:6082
76. Ziman JM. 1962. *Electrons and Phonons: The Theory of Transport Phenomena in Solids*. London: Oxford Univ. Press
77. Roufosse M, Klemens PG. 1973. *Phys. Rev. B* 71:5379–86
78. Leibfried G, Schlomann E. 1954. *Nachr. Ges. Wiss. Goettingen Math. Phys. K. Fachgruppe 1* 2A:71–93

79. Brown JM. 1986. *Geophys. Res. Lett.* 13: 1509–12
80. Yan Y-X, Cheng L-T, Nelson KA. 1988. *J. Chem. Phys.* 88:6477–86
81. Herzfeld KF, Litovitz TA. 1959. *The Absorption and Dispersion of Ultrasonic Waves*. New York: Academic
82. Zaug JM, Slutsky LJ, Brown JM. 1994. *J. Phys. Chem.* 98:6008–16
83. Haar L, Gallagher JS, Kell GS. 1984. *NBS/NRC Steam Tables. Thermodynamic and Transport Properties and Computer Programs for Vapor and Liquid States of Water in SI Units*. Washington, DC: Hemisphere
84. Saul A, Wagner W. 1989. *J. Phys. Chem. Ref. Data* 18:1537–64
85. Lyzenga GA, Ahrens TJ, Nellis WJ, Mitchell AC. 1982. *J. Chem. Phys.* 76: 6282–86
86. Walsh JM, Rice MH. 1957. *J. Chem. Phys.* 26:815–23
87. Mitchell AC, Nellis WJ. 1982. *J. Chem. Phys.* 76:6273–81
88. Jorgensen WL. 1982. *J. Chem. Phys.* 77: 4156–63
89. Brodholt J, Wood B. 1993. *J. Geophys. Res.* 98:519–36
90. Belonoshko A, Saxena SK. 1991. *Geochim. Cosmochim. Acta* 55:381–87
91. Ahrens TJ. 1989. *Nature* 342:122–23
92. Grimsditch M, Popova S, Polian A. 1996. *J. Chem. Phys.* 105:8801
93. Vedam K, Limsuwan P. 1978. *J. Chem. Phys.* 69:4772
94. Schiebener P, Straub J, Levelt-Sengers JMH, Gallagher JS. 1990. *J. Phys. Chem. Ref. Data* 19:677–717
94a. Wiryana S, Brown JM, Slutsky LJ. Manuscript in preparation
95. Krumgalz BS, Pogorelsky R, Iosilevskii YA, Weiser A, Pitzer KS. 1994. *J. Solut. Chem.* 23:849
96. Bradley DJ, Pitzer KS. 1979. *J. Phys. Chem.* 83:1599
97. Nicol M, Hirsch KR, Holzapfel WB. 1979. *Chem. Phys. Lett.* 68:49
98. Abramson EH, Slutsky LJ, Brown JM. 1994. *J. Chem. Phys.* 100:4518–26
99. Deleted in proof
100. Olinger B, Mills RL, Roof RB. 1984. *J. Chem. Phys.* 81:5068
101. d'Amour H, Holzapfel WB, Nicol M. 1981. *J. Phys. Chem.* 85:130
102. Born M, Huang K. 1954. *Dynamical Theory of Crystal Lattices*. Oxford, UK: Oxford Univ. Press
103. Begbie GH, Born M. 1946. *Proc. R. Soc. London Ser. A* 188:179–88
104. Begbie GH. 1946. *Proc. R. Soc. London Ser. A* 188:189–208
105. Etters RD, Kobashi K, Belak J. 1985. *Phys. Rev. B* 32:4097–105
105a. Abramson EH, Slutsky LJ, Harrell MD, Brown JM. Submitted for publication
106. Belonoshko A, Saxena SK. 1991. *Geochim. Cosmochim. Acta* 55:3191–208
107. Stevenson DJ, Salpeter EE. 1977. *Astrophys. J. Suppl.* 35:221–37
107a. Abramson EH, Slutsky LJ, Brown JM. Manuscript in preparation
108. Schiferl D, Cromer KT, Mills RL. 1981. *Acta Cryst.* B37:1329
109. Herbst CA, Cook RL, King Jr. HE. 1993. *Nature* 361:518–20
110. Deleted in proof
111. Roder HM. 1982. *J. Res. Nat. Bur. Stand.* 87:279–310
112. Hemley RJ, ed. 1998. *Ultrahigh-Pressure Mineralogy: Physics and Chemistry of the Earth's Deep Interior*, Vol. 37. Washington, DC: Mineral. Soc. Am.
113. Polian A, Loubeyre P, Boccara N, eds. 1989. *Simple Molecular Systems at Very High Density, NATO ASI Ser. B, Phys.* 186. New York: Plenum